Velocity dependence of single-electron capture for the 0.4−5-keV/amu Ar^{8+}-Cs(6s) collision system

V. Bazin,[1] P. Boduch,[1,2] M. Chantepie,[1,2] G. Cremer,[1,2] E. Jacquet,[1,2] H. Kucal,[1,2] and D. Lecler[1]

[1]*Centre Interdisciplinaire de Recherche Ions Lasers, UMR 6637 CEA-CNRS-ISMRA, Université de Caen, 6 Boulevard Maréchal Juin, F-14050 Caen Cedex, France*
[2]*UFR des Sciences, Université de Caen, F-14032 Caen Cedex, France*

J. Pascale

Service des Photons, Atomes et Molécules, CEA, Centre d'Etudes de Saclay, Bâtiment 522, F-91191 Gif-sur-Yvette Cedex, France

The single-electron capture (SEC) process which occurs in Ar^{8+}-Cs(6s) collisions is experimentally studied, in the 0.4–5-keV/amu energy range, by optical spectroscopy in the near UV and visible wavelength range (200–600 nm). The classical-trajectory Monte Carlo (CTMC) method is also used to determine the state-selective electron-capture cross sections. For high collision energies, strong lines corresponding to $\Delta n = 1-4$ transitions from $n = 7$ to 13 states with large angular momentum values of Ar VIII and $\Delta n = 0$ transitions from $n = 5$ states are observed. For low collision energies, together with the lines observed for high collision energies, lines corresponding to transitions from states with low-l values (10s, 11s, and 13s) are detected. Production cross sections for the most populated levels ($n = 9$, 10, and 11) are determined and compared with the previous experimental data of Martin *et al.* [Phys. Rev. A **46**, 1316 (1992)] and Denis *et al.* [Phys. Rev. A **50**, 2263 (1994)], and with the CTMC calculations. From molecular structure calculations which are performed for the $\{Ar^{7+} + Cs\}^+$ molecular system, our results are analyzed in terms of dynamical couplings between the relevant molecular channels involved in the electron-capture process. Polarization degrees for SEC lines corresponding to transitions between high-l values states are also measured. The comparison with those calculated from the CTMC results provides information about the Zeeman sublevel distributions.

PACS number(s): 34.10.+x, 34.70.+e

I. INTRODUCTION

We study ion-atom collisions in the low-velocity range, typically for the reduced velocity $v \leqslant 1$, which is defined as the ratio of the velocity of the ionic projectile to the initial orbital velocity of the valence electron in the target atom. For these slow collisions between a highly charged ion A^{q+} and a neutral alkali-metal atom target, the main process which occurs is the capture of the active loosely bound electron of the target by the incident ion with a large cross section [1,2]. Numerous studies [1–4] have shown that, because of its high resolution, UV and visible photon spectroscopy is particularly useful in determining the nl-distributions of the most populated levels for A^{q+}+alkali-metal atom collisions. Recently, we have shown [5–8] that it is also possible to have information on m_l distributions using measurements of the polarization rates of the single-electron-capture lines from comparisons with the polarization degrees calculated from $\sigma(nlm_l)$ cross sections determined by using the classical trajectory Monte Carlo (CTMC) method [9–11]. The knowledge of the final nlm_l distributions resulting from the single-electron-capture (SEC) process gives information on the importance of the various coupling mechanisms which take place during the collision. These nlm_l distributions are rather difficult to predict because they depend strongly on the efficiency of the dynamical couplings involved between the relevant electron capture channels and the entrance channel.

We have already studied the effects of the projectile velocity and of the projectile core electrons by studying the

Ar^{8+} and Kr^{8+}-Li(2s) systems [12–14]. To complete our studies, we would like to analyze the effects of the initial alignment of a laser prepared target on the final nlm_l distributions. We have then chosen to study the Ar^{8+}-Cs(6s) and Ar^{8+}-Cs*(6p) systems. The choice of Ar^{8+} ions as projectiles is obvious in continuity with the previous studies. Optical pumping of caesium atoms in the 6p state by means of diode lasers is technically possible. This system was already studied by Martin *et al.* [15] in the 200–500-nm wavelength range and by Denis *et al* [16] in the UV domain. In both papers, the determined cross sections have the same behavior with the energy collision as those obtained from CTMC calculations [17,18], but the order of magnitude of the experimental results are systematically lower than the CTMC results by a factor of about 5 at the peak of the n distribution.

In this manuscript, we present results on single electron capture in Ar^{8+}-Cs(6s) collisions between 0.4 and 5.0 keV/amu. After the description of the experiment (hereafter referred as EXPT1), we present spectroscopic results, wavelengths, and assignments of new SEC observed lines. The emission cross sections are determined from line intensities, the target density, and the optical response of the experimental device for each transition. Production cross sections for the most populated levels ($n = 9$, 10, and 11) are then estimated and compared with the $\sigma(nl)$ cross sections calculated by using the CTMC method and with the experimental results (hereafter referred as EXPT2) of Denis *et al.* [16]. A preliminary theoretical study of the Ar^{8+}-Cs(6s) collision versus the collision energy was already reported [18]. It is
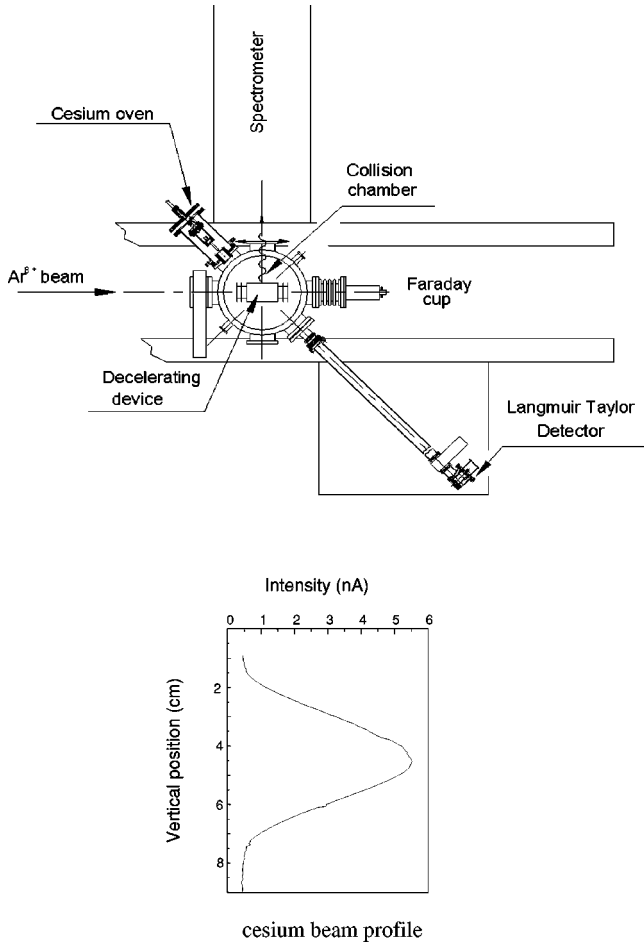
FIG. 1. Experimental setup. A typical cesium beam profile is also included on the figure.

presently implemented and the collision has been analyzed from calculations of the electronic potential energy curves for the $\{Ar^{7+}+Cs\}^+$ molecular system. Polarization rates of single-electron-capture lines corresponding to transitions between high-l values are measured and compared to CTMC results in order to determine the behavior of the m_l distribution versus collision energy.

II. EXPERIMENT

A. Experimental set-up

The experimental setup is presented in Fig. 1. The ion beam is produced by an electron cyclotron resonance ion source at GANIL (Grand Accélérateur National d'Ions Lourds, Caen, France). After a q/m selection, the Ar^{8+} ions are focused onto the center of the collision chamber and collected in a Faraday cup in order to measure the ion-beam intensity, which is of the order of 250 μA.

The caesium beam, whose direction is at 45° from the ion-beam direction, is produced in an oven mainly composed of a copper cylinder chamber. Before the experiment, a small glass tube containing typically 2 g of pure 133 caesium is fixed inside the oven which is heated with a thermocoax wire at a temperature of about 200 °C. When the vacuum inside

the collision chamber is low enough (2×10^{-6} mbar), the caesium tube is broken inside the oven by mean of a piston. In front of the caesium chamber, the nozzle of the oven is composed by a small capillary tube (length 44 mm, diameter 2 mm). In order to prevent caesium scattering, a collimator element composed by two diaphragm slits (6.2×1.4 mm^2) is added. To measure the atomic caesium beam density as function of vertical position, we built a movable Langmuir-Taylor detector [19,20]. This detector is composed of a tungsten wire heated red hot at a temperature of 1800 K and kept at a voltage of $+20$ V. The caesium atoms are all surface ionized by the wire, and are collected by a cathode electrically connected to ground via a picoamperemeter. For each position of the Langmuir-Taylor detector, the current intensity measured by the picoamperemeter gives the flux of caesium atoms which have reached the tungsten wire. A scan over the vertical range results in an intensity profile (cf. Fig. 1). The total flux F is obtained by integrating this profile over the vertical position. The caesium density N can be evaluated for the interaction region with the formula

$$N=\frac{F}{\bar{v}A}=\frac{1}{\varepsilon}\,\gamma\,\frac{1}{e\bar{v}A}\int I_{LT}dz, \tag{1}$$

where ε is the geometric efficiency ($\varepsilon\approx13\%$), γ the ionization efficiency ($\gamma\approx1$), e the absolute value of the electronic charge, d the diameter of the tungsten wire ($d=0.2$ mm), $\bar{v}$ the average velocity of the caesium beam, and A the area of the caesium beam at the collision point ($A=306$ mm^2). The average velocity is optically determined by a method based on the Doppler effect involving two crossed laser beams [21], and is equal to 400 ms^{-1}. The typical density obtained with such a setup is very low, i.e., 10^9 atoms per cm^3. After each Langmuir-Taylor record, the detector is placed into a position corresponding to the maximum of the obtained profile. In first approximation, the intensity measured is proportional to the caesium density evaluated under the profile. This allows to control the target density during the experiment.

Since the investigated energy range was not directly accessible by the ion source, a decelerating device was installed at the vicinity of the collision area. This decelerating device is the same than those described by Laulhé *et al.* [13]. The studied energy domain is then 0.4–5 keV/amu.

The optical device used in this experiment was already described [4,13]. The photons emitted perpendicularly to the direction of the incident ion beam are wavelength analyzed in an horizontal plan by means of a normal incidence grating spectrometer and detected by a photomultiplier in the 200–600-nm wavelength range. A specific wavelength calibration curve was done using a standard mercury lamp, and an Ar VIII line at 433.98$\pm$0.04 nm (wavelength given in air). The wavelength uncertainty is then about 0.08 nm in the second order.

Emission cross sections have been determined from the lines intensities, the relative efficiency curve of the detection (theoretical grating efficiency and phototube response function given by the manufacturer) and the target density mea-

sured by the Langmuir-Taylor detector. The lines intensities have been calibrated by using the spectrum resulting from Ar^{8+}-He collisions recorded with the same optical device [22]. In particular, we have used the emission cross section of the $3s6h$-$3s7i$ transition at 250.05 nm. The relative uncertainties for the strongest lines are estimated to be of the order of $\pm 40\%$. These uncertainties are mainly due to the calibration method and the polarization effects. Since we continually and accurately measure the ion-beam intensity and the target density, we assume that the calibration uncertainties depend mainly on the emission cross section used as reference ($\pm 30\%$). The polarization effects on the determination of the emission cross sections are very difficult to estimate: they depend on the wavelength of the transition, on the diffraction order of the spectrometer grating, and on the polarization of the detected lines. Assuming that the polarization degrees of the Ar VIII emitted lines and the polarization of the line used as reference are of the same order, the uncertainties due to polarization are probably small, and relative uncertainties of $\pm 40\%$ are large enough to include them. Two series of experiments were done. The present results are the average of all experiments.

The polarization degrees P of the emitted lines are determined from the measurements of $I_\parallel$ and $I_\perp$ which are the light intensities with the electric vector parallel and perpendicular to the ion beam direction (taken as the quantization axis), respectively. The polarization degree P is defined by

$$P = \frac{I_\parallel - I_\perp}{I_\parallel + I_\perp}. \tag{2}$$

The polarimeter was already described several times [6,7]. It is composed of two polarizers: a rotating Polacoat for the $I_\parallel$ and $I_\perp$ measurements, and a fixed Glan-Taylor prism to annihilate the polarization effect of the spectrometer.

B. Emission cross sections

Lines due to the single-electron-capture process have been identified in the 200–600-nm wavelength range. They correspond to $\Delta n = 1$–4 transitions from $n=7$ to 13 levels and $\Delta n=0$ transitions from $n=5$ levels. Some of the lines (corresponding to transitions between large l values) observed here were already observed by Martin *et al.* [15] for the same collision system and by Jacquet *et al* [4] and Laulhé *et al.* [13] for the Ar^{8+}-Li($2s$) system. However, 24 new lines have been identified with the help of spectroscopic *ab initio* pseudorelativistic Hartree-Fock (HFR) calculations [23]. These new identifications are listed in Table I. All the emission cross sections for each SEC line are presented in Table II for all collision energies (0.4, 1, 2, 3, 4, and 5 keV/amu).

C. Experimental production cross sections

The production cross section for the state i was determined from emission cross sections

$$\sigma(i) = \sum_{j<i} \sigma_{em}(i \rightarrow j) - \sum_{k>i} \sigma_{em}(k \rightarrow i), \tag{3}$$

TABLE I. New observed lines. (1) Present experimental results. (2) HFR calculations.

Transition	λ_{EXPT} (nm) in air (1)	λ_{HFR} (nm) in vacuum (2)
$8p\,^2P_{3/2}$-$9d\,^2D_{5/2}$	321.72 ± 0.04	321.51
$8h$-$9g$	434.91 ± 0.04	435.13
$9f$-$10g$	602.98 ± 0.08	600.40
$8p\,^2P_{1/2}$-$10s\,^2S_{1/2}$	239.12 ± 0.03	239.49
$8p\,^2P_{3/2}$-$10s\,^2S_{1/2}$	239.76 ± 0.03	240.07
$8d\,^2D_{5/2}$-$10p\,^2P_{3/2}$	268.97 ± 0.03	269.03
$8d\,^2D_{3/2}$-$10p\,^2P_{1/2}$	269.22 ± 0.03	269.30
$8p$-$10d$	207.85 ± 0.03	207.95
$8d$-$10f$	238.90 ± 0.03	238.04
$9p\,^2P_{1/2}$-$11s\,^2S_{1/2}$	334.55 ± 0.04	335.15
$9p\,^2P_{3/2}$-$11s\,^2S_{1/2}$	335.48 ± 0.04	335.93
$9d$-$11f$	328.02 ± 0.04	328.77
$10p$-$12d$	388.76 ± 0.04	389.51
$10f$-$12g$	463.08 ± 0.04	463.03
$10g$-$12h$	464.80 ± 0.04	465.08
$8i,k$-$11k,l$	193.36 ± 0.02	193.44
$9p\,^2P_{3/2}$-$12d\,^2D_{5/2}$	227.03 ± 0.03	226.95
$9f$-$12d$	267.46 ± 0.03	267.58
$9g$-$12h$	263.15 ± 0.03	263.19
$10p\,^2P_{1/2}$-$13s\,^2S_{1/2}$	329.77 ± 0.04	330.58
$10p\,^2P_{3/2}$-$13s\,^2S_{1/2}$	330.27 ± 0.04	331.13
$9d$-$13f$	212.67 ± 0.02	212.99
$9g$-$13h$	221.02 ± 0.02	221.17
$9h,i,k,l$-$13i,k,l,m$	221.32 ± 0.02	221.49

where $\sigma_{em}(i \rightarrow j)$ is the emission cross section corresponding to the transition from the state i to a lower state j, and $\sigma_{em}(k \rightarrow i)$ the emission cross section corresponding to transition from an upper state k to the considered state i. Radiative cascades are taken into account until $n=12$, since we did not observe lines emitted from $n \geq 13$ level (except 9-13 and $10p$-$13s$ transitions which are very weak and not observed for all the collision energies). The emission cross sections for which the wavelength of the associated transition is outside the detection domain can be deduced from known emission cross sections and transitions probabilities. As in previous works [4,13], we used transition probabilities given by Lindgård and Nielsen [24] for configurations with $l \leq 4$, and hydrogenic transition probabilities for configurations with $l \geq 5$. In the case of the lines which contain several transitions with very close wavelengths (unresolved lines), we used the ratios between the corresponding CTMC cross sections to determine the proportion of each component. The production cross sections are given in Table III for the most populated levels, i.e., $9l$, $10l$, and $11l$ together with the corresponding CTMC results (see Sec. IV B). The experimental

TABLE II. Experimental emission cross sections (10^{-16} cm^2) vs projectile energy (keV/amu) for single electron capture in Ar^{8+}-Cs($6s$) collisions. The experimental uncertainties are of 40%.

Transition	λ (nm)	Energy					
		0.4	1.0	2.0	3.0	4.0	5.0
$5p\,^2P_{1/2}$-$5d\,^2D_{3/2}$	302.69	4.0	6.5	4.5	2.9	3.5	1.1
$5p\,^2P_{3/2}$-$5d\,^2D_{5/2}$	306.77	4.7	8.0	7.0	3.8	7.8	0.8
$5s\,^2S_{1/2}$-$5p\,^2P_{3/2}$	392.68	1.9	5.0	3.3	2.5	5.4	1.1
$5s\,^2S_{1/2}$-$5p\,^2P_{1/2}$	400.38	1.4	3.2	1.7	1.2	3.4	0.5
$6g$-$7h$	192.93	25.2	25.5	31.1	23.9	31.4	31.0
$6h$-$7i$	193.09	107.3	109.0	117.0	145.0	121.6	168.4
$7f$-$8g$	294.65				2.8	2.0	
$7g$-$8h$	297.19	10.5	16.3	8.7	14.9	20.3	19.1
$7h,i$-$8i,k$	297.49	275.0	217.8	184.1	387.7	360.1	424.9
metastable $7l$-$8l$	296.59	8.1	6.2	8.2	13.4	16.1	11.8
$8f$-$9g$	429.81	1.3	2.0		1.5	1.8	1.2
$8g$-$9h$	433.49	7.4	5.4	4.8	7.9	6.9	8.2
$8h$-$9i$		22.0	19.3	12.6	25.4		
$8i,k-9k,l$	433.98	228.0	199.6	208.1	308.6	316.4[a]	401.5[a]
metastable $8l$-$9l$	431.95	2.0	9.3	3.1	3.8	3.8	8.1
$9f$-$10g$	602.98						0.8
$9i,k,l$-$10k,l,m$	606.53	127.0	199.3	219.8	259.2	245.7	345.9
$8p\,^2P_{1/2}$-$10s\,^2S_{1/2}$	239.12	4.4	3.7				
$8p\,^2P_{3/2}$-$10s\,^2S_{1/2}$	239.76	6.3	7.5				
$8d\,^2D_{5/2}$-$10p\,^2P_{3/2}$	268.97	4.0	2.9				
$8d\,^2D_{3/2}$-$10p\,^2P_{1/2}$	269.22	2.8	2.1				
$8p$-$10d$	207.85		6.0		1.5		
$8d$-$10f$	238.90		4.6		0.8		
$8f$-$10g$	251.54	4.3	-	3.5	2.0	2.2	1.7
$8g$-$10h$	252.77	4.4	6.3	6.4	13.0	9.0	6.2
$8h$-$10i$	252.92	11.5	14.8	14.3	27.3		30.2
$8i,k$-$10k,l$	253.02	51.9	64.4	64.0	88.9	91.7[b]	103.2
$9p\,^2P_{1/2}$-$11s\,^2S_{1/2}$	334.55	1.1					
$9p\,^2P_{3/2}$-$11s\,^2S_{1/2}$	335.48	0.7					
$9d$-$11f$	328.02	1.3	1.7	2.4			
$9h$-$11i$		2.5	2.9	3.3	4.9		2.5
$9i,k,l$-$11k,l,m$	348.66	12.3	19.2	20.4	30.4	35.5	43.2
$10p$-$12d$	388.76	0.1	2.2				
$10f$-$12g$	463.08	2.6		1.6	3.8	1.2	1.6
$10g$-$12h$	464.80	2.4	2.1	3.2	4.0	2.2	1.6
$10h,i,k,l,m$-$12i,k,l,m,n$	465.75	4.5	3.1	7.9	13.3	13.7	7.7
$8i,k$-$11k,l$	193.36	12.5	23.3	18.7	11.3	15.3	15.1
$9p\,^2P_{3/2}$-$12d\,^2D_{5/2}$	227.03				18.5		
$9f$-$12d$	267.46	2.8	7.9		3.4		
$9g$-$12h$	263.15					2.3	1.3
$9h,i,k,l$-$12i,k,l,m$	263.52	4.3	5.6	5.9	7.3	12.0	13.0
$10p\,^2P_{1/2}$-$13s\,^2S_{1/2}$	329.77	2.0					
$10p\,^2P_{3/2}$-$13s\,^2S_{1/2}$	330.27	3.4					
$9d$-$13f$	212.67		20.5				
$9g$-$13h$	221.02		27.9				5.7
$9h,i,k,l$-$13i,k,l,m$	221.32		22.2				3.1

[a]$8h,i,k$-$9i,k,l$.
[b]$8h,i,k$-$10i,k,l$.

TABLE III. Experimental and CTMC calculated cross sections (10^{-16} cm^2) vs the projectile energy (keV/amu) for single electron capture into the $9l$, $10l$, and $11l$ sublevels for Ar^{8+}-Cs($6s$) collisions.

Energy	0.2		0.4		1.0		2.0		3.0		4.0		5.0
nl	CTMC	EXPT	CTMC	EXPT	CTMC	EXPT	CTMC	EXPT	CTMC	EXPT	CTMC	EXPT	CTMC
$9s$	14.0		13.3		20.9		13.8		8.5		4.1		1.5
$9p$	42.0		53.0		42.3		18.2		12.1		6.7		4.5
$9d$	28.1		27.0		18.6		6.5		4.6		4.1		3.3
$9f$	17.1		12.2		8.2		4.3		2.8		2.3		2.4
$9g$	12.4	10.3	10.3	17.5	9.8		8.2	12.6	7.2	9.9	7.0	7.1	7.3
$9h$	17.9	27.4	14.1	13.5	16.3	15.8	15.7	28.1	15.3	21.4	14.9	23.9	16.2
$9i$	21.9	36.5	18.8	25.5	20.5	9.6	18.3	33.8	23.1	29.3	23.4	36.0	25.1
$9k$	27.6	66.5	35.3	37.2	28.4	15.1	32.3	52.3	30.5	47.7	32.9	46.1	32.0
$9l$	50.1	92.1	51.5	11.3	41.7	11.6	38.0	63.8	34.5	65.5	35.3	45.3	29.5
$10s$	78.5	162.1	73.7	169.2	49.6		16.3		3.6		2.3		1.2
$10p$	172.5	149.4	125.6	108.7	41.1		14.4		7.0		3.3		1.1
$10d$	71.7		37.4		20.6		7.6		4.2		3.8		2.4
$10f$	29.7		17.7		8.2		3.2	21.5	3.5		3.4		3.5
$10g$	24.0	44.6	16.0		14.4	34.3	13.9	18.4	10.6	22.0	8.1	16.7	5.8
$10h$	28.2	23.1	27.5	34.1	22.4	35.6	20.8	17.2	19.0	48.9	16.8	31.7	19.0
$10i$	42.2	30.3	37.6	42.6	45.2	25.3	33.0	39.0	39.6	41.8	40.1	47.3	34.4
$10k$	61.1	47.9	60.8	54.1	56.1	47.2	56.2	70.7	69.9	64.8	70.4	81.6	58.1
$10l$	72.2	60.1	75.4	73.4	73.1	82.8	92.2	106.1	97.4	101.9	98.0	120.2	76.6
$10m$	64.7	55.7	70.1	97.7	97.7	96.6	96.9	103.9	88.3	86.6	76.3	134.2	67.4
$11s$	31.9	34.0	25.1		8.6		1.6		0.7		0.6		0.6
$11p$	32.9		20.1		10.8		6.3		2.6		2.3		1.7
$11d$	15.1		11.2		7.8		5.9		4.0		2.1		1.5
$11f$	8.4	65.8	7.2	77.9	3.5	124.0	3.5		4.8		3.0		2.6
$11g$	6.3		9.3		8.6		7.5		5.9		4.5		3.9
$11h$	12.9		13.3		13.5		10.7		8.2		9.2		10.7
$11i$	11.1	9.8	17.5	10.7	21.1	5.4	18.0	7.2	20.2	8.9	24.8	14.3	24.1
$11k$	12.9	13.9	24.7	15.4	29.7	8.2	26.4	8.2	40.9	18.0	44.5	25.4	37.6
$11l$	8.6	11.0	20.9	14.3	29.0	16.0	52.5	25.9	70.5	27.2	68.5	30.1	47.7
$11m$	8.3	8.6	15.6	19.5	36.0	23.1	74.8	33.4	90.7	35.8	82.5	50.8	73.0
$11n$	4.0		7.2		33.1		72.3		71.1		69.6		80.5

errors for the production cross sections are found to be between 40% and 60%, the theoretical uncertainties are always smaller than 10%.

III. THEORY

A. Classical trajectory Monte Carlo (CTMC) method

In the three-body CTMC method [9–11] the Hamilton's equation of the motion for three classical particles (valence electron plus alkali-metal core Cs$^+$ making the target, ionic core of the projectile Ar^{8+}) are solved, given a set of initial conditions for the target and the projectile. The method of Reinhold and Falcón [25] is used to sample the initial conditions for the target from a microcanonical phase-space distribution. Details on the CTMC method using effective electron-core interactions may be found elsewhere [17,26]. Model potentials are used to describe the interactions between the active electron and each of the ionic cores. For the e^--Cs$^+$ interaction, we use [27]

$$V_{Cs} = -\frac{1}{r}[1 + 54\exp(-3r) + 3.082r\exp(-0.985r)],$$

(4)

and for the e^--Ar^{8+} interaction we use [17]

$$V_{Ar} = -\frac{1}{r}[8 + 10(1 - 1.706r + 1.039r^2)\exp(-3.5r)].$$

(5)

These model potentials were determined to fit spectroscopic data and to have the correct behavior at large and small values of r. The binning procedure of the classical quantities (binding energy, the angular momentum of the electron, and the projection of the angular momentum onto the initial velocity vector of the projectile which is taken as the quantification axis) to determine the final n, l, and m_l quantum numbers of the captured electron was previously described in detail [12,5]. It takes into account the quantum defects of the

TABLE IV. Values of the parameters A_l and B_l for the e^--Cs^+ pseudopotential (see text).

Angular momentum l	A_l	B_l
0	71.242	0.857
1	2.548	0.229
2	-1.152	0.254
$\geqslant 3$	-1.280	0.316

energy levels of the Ar^{7+} ion [28]. Between 1.5×10^4 and 3.5×10^4, trajectories have been used in the calculations to ensure final nl distributions with statistical errors of 3–10 % for the most populated levels ($n = 9$, 10, and 11) while nlm_l distributions have statistical errors of 8–20 % for the most populated nl sublevels.

B. Molecular structure calculations

In order to analyze the variations of the final n, nl, and nlm_l distributions with the projectile energy, the electronic energies of the one-electron $\{Ar^{7+} + Cs\}^+$ molecular system have been calculated using a pseudopotential method from a linear combination of numerical atomic orbitals for Cs and Ar^{7+}. Full details of the method can be found elsewhere [6], where the parameters for the pseudopotential of the e^--Ar^{8+} interaction can be found (note that parameter B2, in Table V of Ref. [6], should be read 8.697 in place of 8.870). For the e^--Cs interaction, we have used

$$V = \sum_l V_l(r) P_l - \frac{1}{r} - 0.5 \alpha_d \frac{r^2}{(r^3 + r_c^3)^2}, \qquad (6)$$

where the value $\alpha_d = 17.82$ a.u. is taken for the static polarizability of Cs^+. The cutoff radius r_c is fixed to 1.989 a.u., which is the value of the Cs^+-core radius [29]. P_l is an angular momentum projector on the Cs^+ core, and $V_l(r)$ is a Gaussian-type pseudopotential:

$$V_l(r) = A_l \exp(-B_l r^2). \qquad (7)$$

The values taken for A_l and B_l can be found in Table IV. In the atomic basis state expansion of the total electronic wave function for the $\{Ar^{7+} + Cs\}^+$ system, all the nl radial wave functions for the Ar^{7+} ion from the ground state $n = 3$ up to the $n = 17$ level have been considered. For the Cs atom, we have considered the ns ($n = 6$–7), np ($n = 6$–8), nd ($n = 5$–7), nf ($n = 4$–5), and $5g$ radial wave functions. Note that the parameters of the e^--core interactions were determined by numerically solving the one-electron Schrödinger radial equations to fit the two lowest energies of each nl series of Ar^{7+} and Cs.

The core-core interaction, mainly the $8/R$ repulsive interaction, has not been included in the calculations, since it does not contribute to the non-adiabatic couplings between the molecular states. The electronic energies of the $\{Ar^{7+} + Cs\}^+$ molecular system have been calculated for the Σ and Π symmetries in the internuclear distance range $R = 15$–70
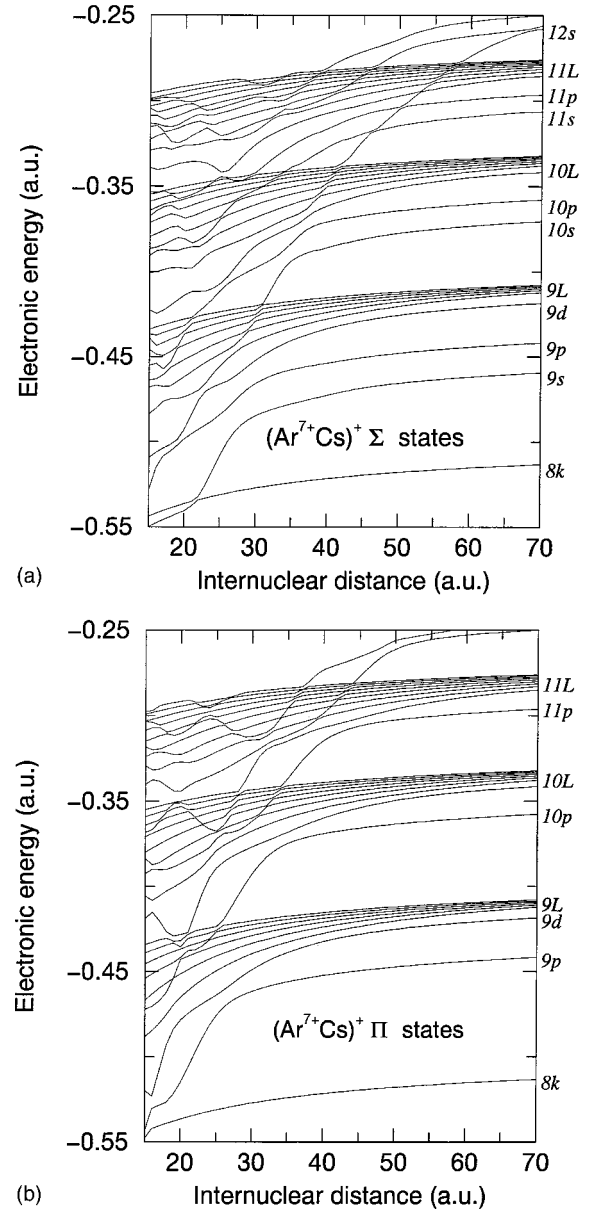

FIG. 2. Electronic energies (in atomic units) vs the internuclear distance (in atomic units) for the $\{Ar^{7+} + Cs\}^+$ system. (a) Σ states, (b) Π states.

a.u. Those relevant to the main capture channels (corresponding to the $n = 9$, 10, and 11 levels) are reported in Figs. 2(a) and 2(b).

In Fig. 2(a), the uppermost Σ energy curve above the manifold of electronic energy curves correlating to the $n = 11$ level of Ar^{7+} is the entrance channel $\Sigma(6s)$ which, through numerous nearby crossings, goes to the $6s$ configuration of Cs at large internuclear distances. This $\Sigma(6s)$ entrance channel crosses nearly diabatically the manifold of Σ_{nl} exit channels, correlating at large R with the nl levels of Ar^{7+} ($n = 9$ and 10 with $l \geqslant 4$, and $n = 11$ for all l values) while it shows up avoided crossings with significant energy splittings with the exit channels Σ_{9l} and Σ_{10l} ($l \leqslant 3$) in the range $R \cong 27$–29 and 34–38 a.u., respectively. These avoided crossings are responsible for primary radial cou-

plings leading to electron capture into the $n=9$ and 10 levels. They are also responsible for the so-called projectile-core-electron effect to populate low-l values at low energies. Other avoided crossings with significant energy splittings are also observed between exit channels at smaller internuclear distances (between the Σ_{9p} and Σ_{9d} channels at $R\cong18$ a.u., between the Σ_{9d} and Σ_{9f} channels at $R\cong23$ a.u., and between the Σ_{10p} and Σ_{10d} channels at $R\cong25$ a.u.). A smooth avoided crossing between the Σ_{9d} and Σ_{9f} exit channels can be seen in the range $R\cong45-55$ a.u. After the primary radial couplings which populate the low values of l, and in addition to the Stark effect due to the residual ion and the intrashell rotational couplings [see the previous discussion [6,7,13] for the Ar^{8+}-Li(2s) collisions], these avoided crossings should contribute to the population of the nl and nlm_l sublevels by radial couplings. We have already noted that the $\Sigma(6s)$ entrance channel crosses nearly diabatically all the Σ_{11l} exit channels, and especially the Σ_{11l} exit channels with low-l values, while the $n=11$ level becomes the most populated level at the largest energies (see below). For the population of this capture level and higher ones, intershell rotational couplings have to be invoked, since no primary radial coupling relevant to these levels will be sufficiently efficient. For this, let us consider the Π energy curves in Fig. 2(b).

In order to be efficient, the Π exit channels have to be populated in the first place by rotational coupling with the $\Sigma(6s)$ entrance channel. This is possible in the region of internuclear distances where the $\Sigma(6s)$ entrance channel shows avoided crossings with the exit channels Σ_{nl} ($n=9$ and 10; $l\le3$). Thus, after the primary radial couplings, Π_{9l} and Π_{10l} exit channels may be populated by rotational couplings with the Σ_{10l} and Σ_{9l} exit channels (low-l values). The potential energy curve correlating through numerous nearly crossings to the 6p configuration of Cs, and that we call $\Pi(6p)$, shows up avoided crossings with exit channels Π_{np} for $n=9$, 10, and 11 at $R\cong25$, 30, and 40 a.u., respectively. Moreover, other avoided crossings are also observed between the Π_{np} and Π_{nd} ($n=9-11$) exit channels at $R\cong27$, 35, and 45 a.u., respectively. The avoided crossings between these exit channels and the $\Pi(6p)$ channel should contribute by radial coupling to the electron capture into the np and nd configurations, and also to the higher values of l by Stark effect and intrashell rotational coupling. The 11s configuration is populated by rotational coupling between $\Pi(6p)$ and Σ_{11s} channels.

Obviously the Π channels may also contribute to electron capture into the $n=9$ and 10 levels; however, for these levels, primary radial couplings are predominant. For the population of the $n=11$ level, rotational couplings become the predominant coupling. Consequently, one should expect that the total cross section for capture into the $n=11$ level increases with the energy, while the total cross sections for capture into the $n=10$ and 9 levels should decrease or go through a maximum [6] ; the energy position of this maximum varying with the energy splitting at the avoided crossing between the $\Sigma(6s)$ and Σ_{nl} exit channels. Finally, it is worth noting that the maximum impact parameter b which contributes to the total electron capture cross section (see
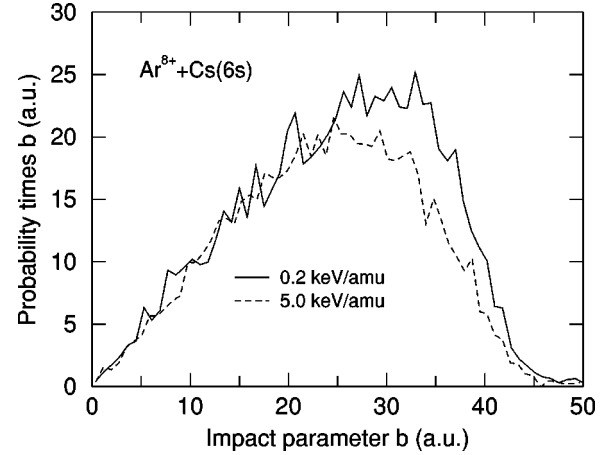

FIG. 3. CTMC calculated probability times b vs impact parameter b for total electron capture in Ar^{8+}-Cs(6s) collisions at projectile energies of 0.2 and 5 keV/amu, as indicated in the figure.

Fig. 3) agrees with the internuclear range of primary radial couplings responsible for the one-electron capture.

IV. RESULTS AND DISCUSSIONS

A. Total electron-capture cross sections and final n distribution

Since only lines emitted in the near UV and visible wavelength range are detected, it is not possible to determine experimental n distributions, and we discuss the CTMC ones. The CTMC cross sections $\sigma(n)$ for an electron into a specific n level are reported in Table V for the 0.2–5-keV/amu energy range, along with the total electron capture $\sigma_{tot}=\Sigma_n\sigma(n)$. The σ_{tot} cross section is almost constant over all the energy range. The very slight increase of the cross section with decreasing energies is due to successive increasing efficiency of the primary radial couplings to populate the low values of l at low energies. Indeed, the maximum of the probability for total electron capture times the impact param-

TABLE V. CTMC calculated cross section (10^{-15} cm^2) vs projectile energy (keV/amu) for single-electron capture into n levels of Ar^{7+} from Cs(6s). The total electron cross section (10^{-15} cm^2) and the reduced total electron-capture cross section (10^{-15} cm^2) are also reported.

Energy	0.2	0.4	1.0	2.0	3.0	4.0	5.0
n							
7	0.2	0.5	0.7	1.1	1.3	1.3	1.4
8	2.7	4.0	5.6	4.9	4.2	4.2	4.4
9	23.1	23.6	20.7	15.5	13.9	13.1	12.2
10	64.5	54.2	42.8	35.5	34.3	32.2	27.0
11	15.0	17.2	20.2	27.9	32.0	31.1	28.4
12	1.9	2.7	4.1	7.2	6.6	8.4	12.5
13	0.3	0.9	1.9	3.0	1.9	2.0	3.0
Total	110.0	106.1	99.8	99.6	98.6	96.2	93.6
Reduced	1.13	1.09	1.02	1.02	1.01	0.98	0.96

eter b (see Fig. 3) increases only slightly with decreasing energies while the maximum position is shifted to larger impact parameters. The reduced total electron-capture cross section [30]

$$\sigma_{tot}^r = \frac{4I_t}{q}\sigma_{tot},\qquad(8)$$

where I_t is the ionization potential of the target and q the charge of the projectile, is also reported in the Table V. It varies from 0.96×10^{-15} cm^2 at 5 keV/amu to 1.13×10^{-15} cm^2 at 0.2 keV/amu, in agreement with the scaling formula of Schweinzer *et al.* [30], which predicted a value of 0.9×10^{-15} cm^2 over this entire energy range. This is also in agreement with the results obtained for the Ar^{8+}-Li(2s) collision [6] and for the Kr^{8+}-Li(2s) collision [14] for the same energy range.

As seen in Table V, the most populated levels are the $n=9$, 10, and 11 ones. The n distribution is mainly peaked at $n=10$ in the 0.2–1-keV/amu energy range. The distribution enlarges with increasing energy and the maximum of the n distribution is shifted to $n=11$ at largest energies. As expected from the above discussion (see Sec. III B) the cross section $\sigma(n=10)$ increases continuously with decreasing energy due to more efficient primary radial couplings to populate the low values of l. For total capture into $n=9$, the relevant energy splittings are larger comparatively to those for the capture into the $n=10$ level, so that the cross section $\sigma(n=9)$ has a flat maximum at the lowest energies, and then decreases continuously above 0.4 keV/amu. In contrast, the $\sigma(n)$ cross sections for $n=11$, 12, and 13 increase continuously with increasing energy due to more efficient rotational couplings.

B. Final nl distributions

As seen in Table III, the CTMC calculations are in good agreement with the present experimental results both for the behavior of the nl distribution versus the collision energy and for the absolute values of the cross sections except for four configurations ($10s$, $9k$, $9l$, and $11f$). Figures 4(a) and 4(b) show these comparisons more clearly for $10l$ distribution at 0.4 and 5.0 keV/amu. The results of Denis *et al.* [16] (EXPT2) are also reported in Fig. 4(a), with a multiplicative factor of 3, showing a good agreement with the CTMC results, except for the $10s$ cross section. This indicates that the experimental cross sections determined by these authors are probably underestimated.

As already noted by Denis *et al.* [16] and also by Gauntt and Danzmann [2] for the Ar^{8+}+Na(3s) collision in the 0.04–0.09-keV/amu energy range (where the main capture channel is $n=9$), our experimental and theoretical results agree to find a strong projectile-core electron effect at low energies, which leads to much higher populations in the $l=0$ and 1 levels than in the higher values of l. Our experimental results (EXPT1) find a $10l$ distribution which is peaked on the $10s$ level, while our CTMC calculated $10l$ distribution is peaked on the $10p$ level. Because of experimental errors, this difference has to be considered carefully.
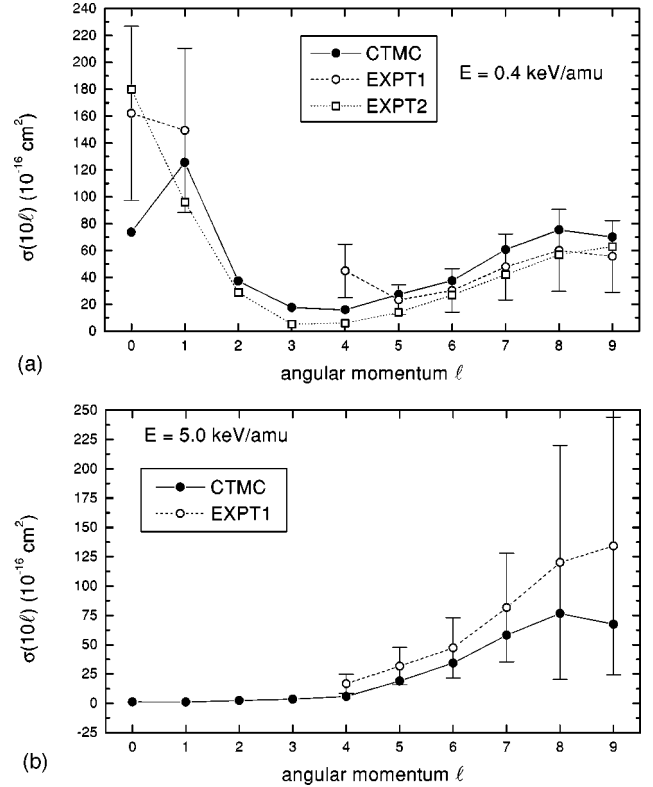

FIG. 4. Comparisons between CTMC calculated (full circle) and experimental (open symbols) $\sigma(10l)$ electron-capture cross sections vs the angular momentum l at 0.4 keV/amu (a) and 5.0 keV/amu (b). EXPT1: present experimental results. EXPT2: experimental results of Denis *et al.* reported with a multiplicative factor of 3. The curves have been drawn to guide the eye. Because of the scale, theoretical uncertainties which are smaller than 10% are not indicated.

Nevertheless, in EXPT2 of Denis *et al.* [16], the maximum of the $10l$ distribution is also found for the $10s$ level. Moreover, for the Ar^{8+}+Na(3s) collision, Gauntt and Dauzmann [2] found a $\sigma(9s)$ cross section which is larger than the $\sigma(9p)$ cross section at low energies. For the Ar^{8+}-Li(2s) system, Laulhé *et al.* [6] found the same result contrary to the CTMC calculations. Thus, it is also worth noting the semiclassical close-coupling calculations of Harel and Jouin [31] for the Ar^{8+}+H(1s) collision in the 1–16-keV/amu energy range. For that collision, where the main capture channel is $n=5$, the population of the $5s$ level never exceeds that of the $5p$ level; the $\sigma(5s)$ cross section has a maximum near 4 keV/amu and the $\sigma(5p)$ cross section a maximum near 2.3 keV/amu. Comparatively, our CTMC calculations find a maximum for $\sigma(10s)$ in the energy range near 0.2–0.4 keV/amu, while the maximum for the $\sigma(10p)$ is probably below 0.2 keV/amu. This is in agreement with the projectile-core electron effect which results from primary radial couplings at the avoided crossings between the Σ entrance channel, and the various Σ channels leading to electron capture into nl levels with low l.

As discussed above (Sec. III) and in our previous studies on Ar^{8+}+Li(2s) [6] and Kr^{8+}+Li(2s) collisions [14], the position of the maximum in the $\sigma(nl)$ (low l) cross sections should be shifted to smaller energy with increasing l, or with
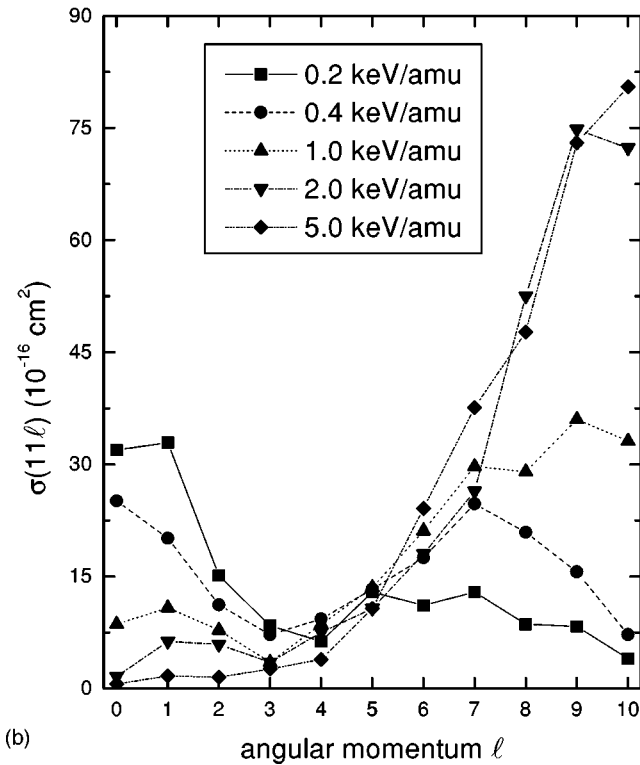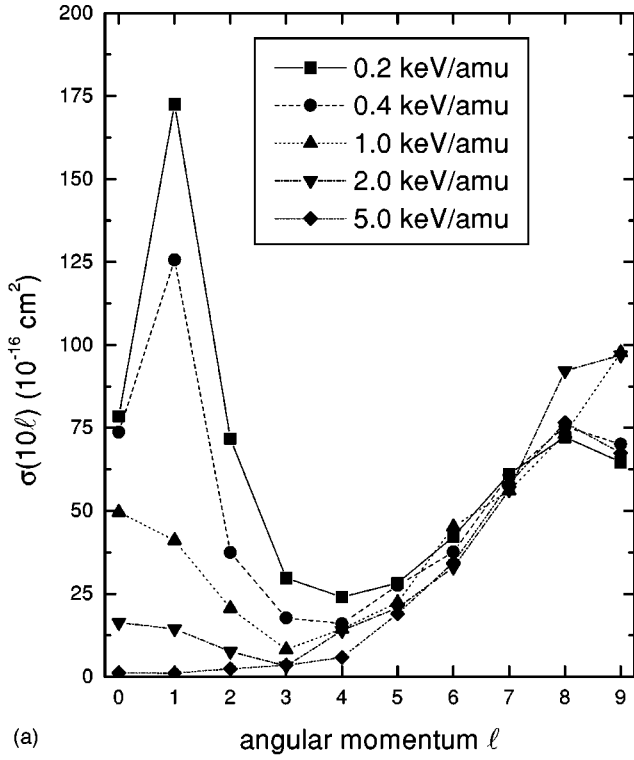
(a)

(b)

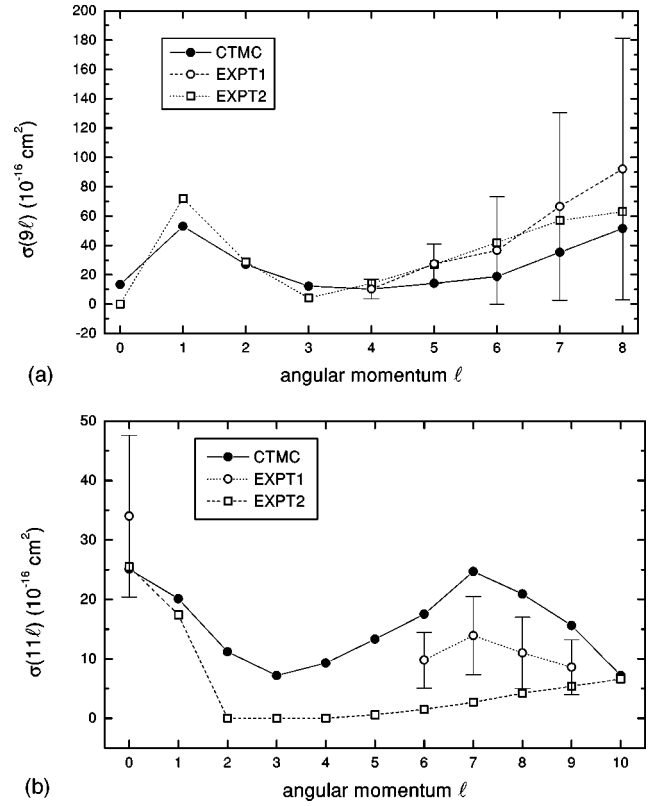FIG. 6. Comparisons between CTMC calculated (full circles) and experimental (open symbols) $\sigma(nl)$ electron-capture cross sections vs the angular momentum l at 0.4 keV/amu for $n=9$ (a) and $n=11$ (b). EXPT1: present experimental results. EXPT2: experimental results of Denis *et al.* reported with a multiplicative factor of 3. The value of $\sigma(11f)$ is not indicated on the figure (see the text).

(a)

(b)

FIG. 5. CTMC calculated $\sigma(nl)$ electron-capture cross sections vs the angular momentum l at different projectile energies (as indicated in the figure) for $n=10$ (a) and $n=11$ (b).

increasing n for l fixed. This is better seen in Table III and in Fig. 5(a), where the CTMC calculated $\sigma(9s)$ cross section has a maximum near 1 keV/amu, while the $\sigma(9p)$ cross section is maximum near 0.4 keV/amu; the $\sigma(9d)$ cross sec-

tion has a maximum in the 0.2–0.4-keV/amu energy range while the $\sigma(10d)$ probably has its maximum below 0.2 keV/amu. Note that above 1 keV/amu, the CTMC calculated $\sigma(10s)$ cross section becomes larger than the $\sigma(10p)$ cross section, which may be expected because the $n=10$ level is the most populated level, and the primary radial coupling between the Σ entrance channel and the Σ channel, leading to electron capture into the $10s$ level, is the first radial coupling to become efficient when the energy decreases. Also note that, at low energies, the $\sigma(9p)$ cross section has values as large as for the highest l values. This can be seen in Fig. 6(a) where, at an energy of 0.4 keV/amu, the CTMC calculated $9l$ are found in qualitative agreement with the experimental results of Denis *et al.* [16] (within a multiplicative factor of 3). Finally, it is worth noting that the $\sigma(nl)$ cross sections for high values of l do not vary much over the entire energy range, except maybe for the largest l values in the $9l$ and $10l$ configuration [see Table III and Fig. 5(a)]. Indeed, for $n=9$ or 10, the large values of l are populated by the Stark effect and rotational coupling after the primary radial couplings which populate the low values of l. In contrast, the $\sigma(11l)$ cross sections have very different behavior with energy. As the energy decreases, the low values of l ($l\leqslant3$) become more and more populated, but to the detriment of the

highest values of l [see Fig. 5(b)]. As seen in Fig. 6(b), at an energy of 0.4 keV/amu, the CTMC calculated 11l distribution is found to be in qualitative agreement with our experimental data, except for the $\sigma(11f)$ cross section. As discussed above (Sec. III), the Σ_{11l} capture channels do not show up avoided crossings with the $\Sigma(6s)$ entrance channel, so that primary rotational couplings between the entrance channel and Π channels have been invoked to populate the 11l levels (and higher ones) with low values of l. The populations of these levels are then redistributed by a post-Stark effect and rotational couplings to the large value of l with increasing energy. In conclusion, the 11l configurations with low values of l are mainly populated at low energy, while their population is then quickly redistributed to large values of l with increasing energy.

Let us discuss the other disagreements observed between the CTMC results and the experimental data concerning the 9k and 9l configurations at 1 and 2 keV/amu, and the 11f configuration at 0.4, 1, and 2 keV/amu (Table III). They can be explained in the following way.

For the 9k and 9l configurations, the corresponding observed line at 433.98 nm contains three transitions: 8h-9i, 8i-9k, and 8k-9l. In order to estimate the ratio between $\sigma_{em}(8h\text{-}9i)$, $\sigma_{em}(8i\text{-}9k)$, and $\sigma_{em}(8k\text{-}9l)$, we have used the corresponding ratio deduced from CTMC emission cross sections. However, at 1 and 2 keV/amu the intensity of the line must be underestimated, and since the cascade effect from $n=10$, the most populated level, is important, the $\sigma(9k)$ and $\sigma(9l)$ cross sections are certainly too weak.

For the 11f configuration, the cross section mainly depends on the determination of the 9d-11f line intensity, as shown in the following formula:

$$\sigma(11f) = \frac{\sigma(11f \rightarrow 9d)}{0.019} - 0.755\sigma(12g \rightarrow 10f). \quad (9)$$

The line corresponding to the 9d-11f transition is observed for 0.4-, 1-, and 2-keV/amu collision energies. In the three spectra, this line is very weak and its intensity can easily be overestimated. The associated branching ratio being also very weak, we obtain an amplification of this overestimation for the considered configuration. Because of this overestimation, the value of $\sigma(11f)$ for 0.4 keV/amu is not reported in Fig. 6(b).

C. Polarization degrees of lines and final nlm_l distributions

The intensities of the observed lines corresponding to transitions between low-l value states ($l=0$ and 1) are very weak, and their polarization degrees P are zero or almost zero [6,7]. Since lines corresponding to transitions between intermediate-l values have also weak intensities, it was only possible to determine P for transitions between high-l values.

The experimental and CTMC calculated polarization degrees of lines versus the collision energy are reported in Figs. 7(a) and 7(b) for the $8h,i,k$-$9i,k,l$ and $9h,i,k,l$-$11i,k,l,m$ transitions. Details of the calculation of polarization rates from CTMC calculated $\sigma(nlm_l)$ cross sections can be found elsewhere [6,8]. The CTMC calculated polarization
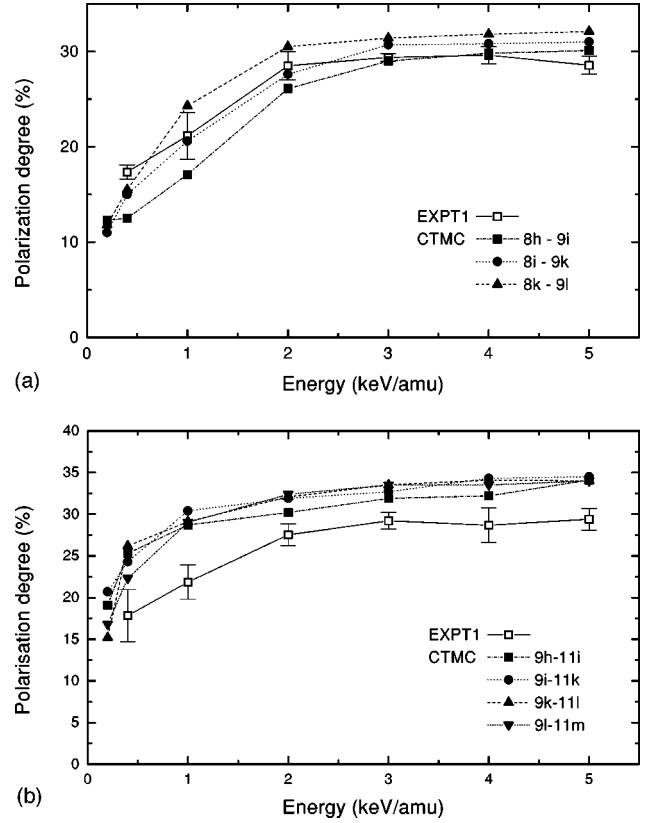

FIG. 7. Comparisons between experimental (open symbols) and theoretical (full symbols) polarization degrees of lines for the $8h,i,k$-$9i,k,l$ (a) and $9h,i,k,l$-$11i,k,l,m$ (b) transitions, as indicated in the figure.

rates indicated in Figs. 7(a) and 7(b) include radiative cascade effects up to $n=12$. A fair agreement is observed between experimental and calculated data for both the energy variation and the absolute values. The polarization degrees increase more or less quickly with energy (from about 10% for the $8h,i,k$-$9i,k,l$ transition) to reach values of nearly 30% for all the transitions. These polarization degrees are consistent with the CTMC calculated nlm_l distributions which show, for these transitions from sublevels with large l values, significant populations of large m_l values at low energies, and then a population of mainly $m_l \leq 4$ at the largest energies. For the transitions from nl sublevels with the lowest l values, the cascades from the upper levels should increase the polarization of these transitions at the lowest energies since they originate from nl sublevels with large values of l [13,8]. Because of space it is not possible to report these nlm_l distributions. However, we note that for transitions from nl sublevels with low l (in particular for $l \leq 4$), the CTMC calculated nlm_l distributions indicate that the polarization degrees should take negative or small values at low energies, to increase more or less quickly at large energies.

V. CONCLUSION

By means of photon emission spectroscopy and CTMC calculations, we have studied single electron capture in

Ar^{8+}-Cs($6s$) collisions between 0.4 and 5 keV/amu. From a spectroscopic point of view, 24 new lines have been observed. From line intensities, emission cross sections have been determined. Production cross sections for the $n = 9$, 10, and 11 levels have been presented and compared with CTMC calculations and experimental results of Martin *et al.* [15] and Denis *et al.* [16]. A specific attention has been paid to the most populated level ($n = 10$): the obtained $10l$ distribution confirms the very strong projectile core electron effect observed at low energy by Martin *et al.* [15] and Denis *et al.* [16], and also found by preliminary CTMC calculations [18]. The behavior of this $10l$ distribution versus energy collision is the same as those observed by Laulhé *et al.* [13] on Ar^{8+}-Li system: at high energy, only high-l value states are populated and at low energy, due to the effect of the electron core of the projectile, low-l value states ($l = 0$ and 1) are populated to the detriment of high-l value states. Both the experimental and CTMC calculated results have been analyzed in terms of dynamical couplings by using calculations

of the electronic energies of one-electron $\{Ar^{7+} + Cs\}^+$ system. The polarization degrees of Ar^{7+}-ion emission lines resulting from transitions between high-l value states have been measured and compared with fair agreement with theoretical ones obtained from CTMC calculated $\sigma(nlm_l)$ cross sections. The increase of the polarization degrees with projectile energies indicates that, after the collision, the electronic cloud tends to be more aligned parallel to the incident ion-beam direction. In other words, it means that the m_l distributions of the nl produced states are more and more peaked on $m_l = 0$, 1, and 2 when the projectile energy increases.

ACKNOWLEDGMENTS

[1] D. Dijkkamp, A. Brazuk, A. G. Drentje, F. J. de Heer, and H. Winter, J. Phys. B **17**, 4371 (1984).

[2] D. M. Gauntt and K. Danzmann, Phys. Rev. A **46**, 5580 (1992).

[3] E. Wolfrum, R. Hoekstra, F. J. de Heer, R. Morgenstern, and H. Winter, J. Phys. B **25**, 2597 (1992).

[4] E. Jacquet, P. Boduch, M. Chantepie, M Druetta, D. Hennecart, X. Husson, D. Lecler, R. E. Olson, J. Pascale, N. Stolterfoht, and M. Wilson, Phys. Scr. **47**, 618 (1993).

[5] C. Laulhé, E. Jacquet, G. Cremer, J. Pascale, P. Boduch, G. Rieger, D. Lecler, M. Chantepie, and J. L. Cojan, Phys. Rev. A **52**, 3803 (1995).

[6] C. Laulhé, E. Jacquet, G. Cremer, J. Pascale, P. Boduch, G. Rieger, M. Chantepie, and D. Lecler, Phys. Rev. A **55**, 1088 (1997).

[7] C. Laulhé, E. Jacquet, P. Boduch, M. Chantepie, G. Cremer, N. Gherardi, X. Husson, D. Lecler, and J. Pascale, J. Phys. B **30**, 1517 (1997).

[8] E. Jacquet, H. Kucal, V. Bazin, P. Boduch, M. Chantepie, G. Cremer, C. Laulhé, D. Lecler, and J. Pascale, Phys. Rev. A **62**, 022712 (2000).

[9] R. Abrines and I. C. Percival, Proc. Phys. Soc. London **88**, 861 (1966).

[10] R. Abrines and I. C. Percival, Proc. Phys. Soc. London **88**, 873 (1966).

[11] R. E. Olson and A. Salop, Phys. Rev. A **16**, 531 (1977).

[12] E. Jacquet, J. Pascale, P. Boduch, M. Chantepie, and D. Lecler, J. Phys. B **28**, 2221 (1995).

[13] C. Laulhé, E. Jacquet, P. Boduch, M. Chantepie, N. Gherardi, X. Husson, D. Lecler, and J. Pascale, J. Phys. B **30**, 2899 (1997).

[14] E. Jacquet, M. Chantepie, P. Boduch, C. Laulhé, D. Lecler, and J. Pascale, J. Phys. B **32**, 1151 (1999).

[15] S. Martin, A. Denis, Y. Ouerdane, M. Carré, M. C. Buchet-Poulizac, and J. Désesquelles, Phys. Rev. A **46**, 1316 (1992).

[16] A. Denis, S. Martin, L. Chen, and J. Désesquelles, Phys. Rev. A **50**, 2263 (1994).

[17] J. Pascale, R. E. Olson, and C. O. Reinhold, Phys. Rev. A **42**, 5305 (1990).

[18] J. Pascale (unpublished).

[19] J. Taylor and I. Langmuir, Phys. Rev. **44**, 423 (1933).

[20] B. Schlatmann, thesis, University of Groningen, 1993.

[21] W. Demtröder, *Laser Spectroscopy (Basic Concepts and Instrumentation)* (Springer-Verlag, Berlin, 1988), p. 472.

[22] P. Boduch, M. Chantepie, D. Hennecart, X. Husson, H. Kucal, D. Lecler, N. Stolterfoht, M. Druetta, B. Fawcett, and M. Wilson, Phys. Scr. **45**, 203 (1992).

[23] R. D. Cowan, *The Theory of Atomic Structure and Spectra* (University of California Press, Berkeley, 1981).

[24] A. Lindgård and S. E. Nielsen, At. Data Nucl. Data Tables **19**, 563 (1977).

[25] C. O. Reinhold and C. A. Falcón, Phys. Rev. A **33**, 3859 (1986).

[26] R. E. Olson, J. Pascale, and R. Hoekstra, J. Phys. B **25**, 4241 (1992).

[27] M. Klapisch, Comput. Phys. Commun. **2**, 239 (1971).

[28] C. E. Theodosiou, M. Inokuti, and S. T. Manson, At. Data Nucl. Data Tables **35**, 473 (1986).

[29] J. P. Desclaux, At. Data Nucl. Data Tables **12**, 311 (1973).

[30] J. Schweinzer, D. Wutte, and H. Winter, J. Phys. B **27**, 137 (1994).

[31] C. Harel and H. Jouin, J. Phys. B **21**, 859 (1988).